Amorphous Mixtures of Ice and C_{60} Fullerene

Siriney O. Halukeerthi,[a] Jacob J. Shephard,[a,b] Sukhpreet K. Talewar,[a] John S. O. Evans,[b] Alexander Rosu-Finsen,[a] Christoph G. Salzmann[a]*

[a] Department of Chemistry, University College London, 20 Gordon Street, London WC1H 0AJ, United Kingdom.

[b] Department of Chemistry, Durham University, South Road, Durham DH1 3LE, United Kingdom.

Corresponding Author

* email: c.salzmann@ucl.ac.uk, tel: +44 7679 8864

Abstract

Carbon and ice make up a substantial proportion of our Universe. Recent space exploration has shown that these two chemical species often coexist including on comets, asteroids and in the interstellar medium. Here we prepare mixtures of C_{60} fullerene and H_2O by vapor co-deposition at 90 K with molar C_{60}:H_2O ratios ranging from 1:1254 to 1:5. The C_{60} percolation threshold is found between the 1:132 and 1:48 samples, corresponding to a transition from matrix-isolated C_{60} molecules to percolating C_{60} domains that confine the H_2O. Below this threshold, the crystallization and thermal desorption properties of H_2O are not significantly affected by the C_{60}, whereas the crystallization temperature of H_2O is shifted towards higher temperatures for the C_{60}-rich samples. These C_{60}-rich samples also display exotherms corresponding to the crystallization of C_{60} as the two components undergo phase separation. More than 60 volume percent C_{60} is required to significantly affect the desorption properties of H_2O. A thick blanket of C_{60} on top of pure amorphous ice is found to display large cracks due to water desorption. These findings may help understand the recently observed unusual surface features and the H_2O weather cycle on the 67P/Churyumov–Gerasimenko comet.

Introduction

Vapor-deposited amorphous ice, traditionally called amorphous solid water (ASW),[1-2] is the most abundant form of H_2O in the Universe.[3-7] The reactive accretion of H and O atoms onto dust grain surfaces is the dominant formation pathway for ice in the interstellar medium.[8] Such grain surfaces are mainly silicate- or carbon-based as evidenced from astronomical spectra.[3] The dominant carbon species in space are polycyclic aromatic hydrocarbons (PAHs) and fullerenes.[3,9-11] The Long Duration Space Exploration mission observed fullerene residues on the panels of the spacecraft[12] and they have also been found in the Allende meteorite.[13] C_{60} and other fullerenes are considered to be the stable end members of astrochemical reaction cascades involving reactive carbon species such as PAHs.[14]

Carbon species and ice have been found to coexist with H_2O in a variety of settings. Notably, NASA's deep impact mission proved the coexistence of PAHs and ice in the Tempel 1 comet.[15] As part of ESA's Rosetta mission, the Philae probe landed on the surface of the 67P/Churyumov–Gerasimenko comet. The dark appearance of 67P is attributed to a 'carbon blanket' on top of a nucleus composed of ices, organic materials and minerals.[16-18] The presence of unique surface features such as 'pits' and 'goosebumps' was attributed to complex weather cycles arising from consecutive water desorption and re-condensation cycles.[19-20] Future developments will include sample-return missions by the OSIRIS-REx and Hayabusa2 spacecrafts from the carbon-rich asteroids Bennu and Ryugu, respectively.[21-22] Such asteroids could provide an interesting window into the past of the solar system. In addition to future advances in space exploration, lab-based studies into the physical properties of carbon / ice mixtures are needed to fully understand the properties of these primordial materials.

The vast majority of studies into mixtures of ASW with other materials to date have

focused on so-called "gas-laden amorphous ices".[23-26] Guest species with lower volatilities have included PAHs, and a variety of studies exploring the spectroscopic and photochemical properties of PAH / ASW mixtures have been reported.[27-32] Benzene has served as a PAH analogue in a variety of studies.[33-36] The aggregation of pyrene as a consequence of the crystallization of the ASW matrix was investigated spectroscopically[37] and matrix-isolated 2-naphthol was used as a spectroscopic probe for investigating the molecular mechanism of the glass transition of ASW[38] which is governed by reorientation dynamics.[39-40]

Here we prepare mixtures of amorphous ice and C_{60} fullerene, the guest species with the lowest volatility investigated so far. C_{60} is used as a 'dust' analogue thought to resemble the dark carbon species identified, for example, on the surfaces of comets and asteroids. Using calorimetry, X-ray diffraction and temperature-programmed desorption experiments, the effect of C_{60} on the crystallization and desorption properties of amorphous ice is investigated across a large composition range.

Experimental Methods

Cryogenic co-deposition of C_{60} fullerene and water vapor

The experimental setup for cryogenic vapor deposition was based on a $12 \times 12 \times 24$-inch box vacuum chamber from Kurt Lesker as shown schematically in Fig. 1(a). Full details on the setup are given in refs 26, 39, 41. For this study, the vacuum chamber was additionally fitted with an LTE-10 point source evaporator deposition source from Kurt Lesker equipped with a pneumatically controlled shutter. For each experiment, about one gram of C_{60} fullerene powder from Tokyo Chemical Industry UK Ltd was placed inside the 15 cm^3 Al_2O_3 crucible of the evaporation source and gently compacted with a piston. The temperature of the evaporation

4

source was measured with a K-type thermocouple and controlled with a Eurotherm 2408 PID unit which is part of a MAPS power supply from Kurt Lesker.
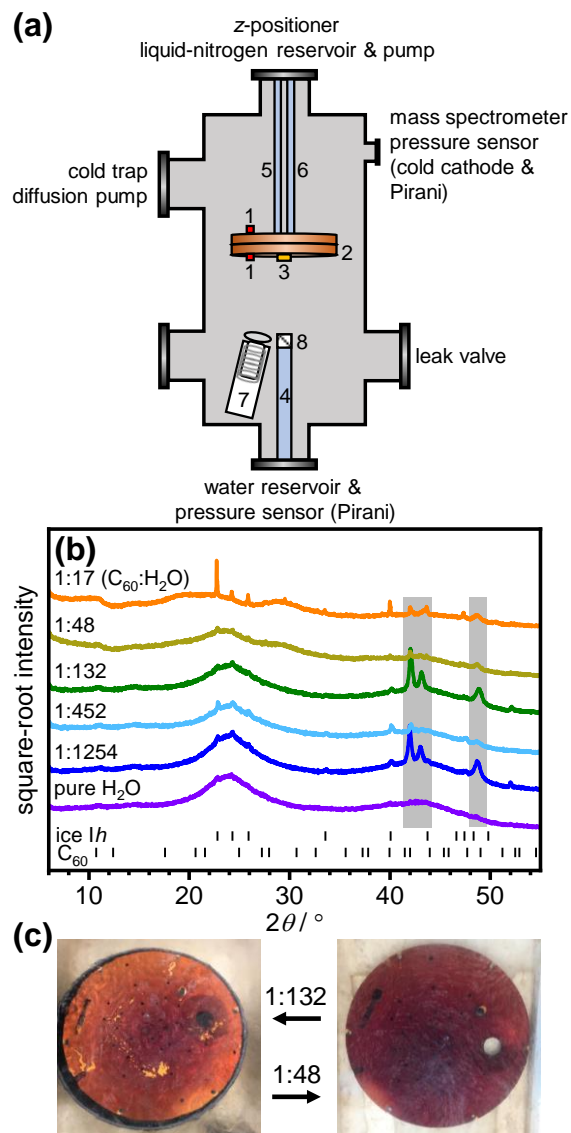
Figure 1. *(a) Schematic illustration of the experimental setup for cryogenic co-deposition of C_{60} fullerene and water vapor. A range of accessories are connected to the ports of the vacuum chamber as indicated. The components inside the chamber are (1) K-type thermocouple temperature sensors, (2) cryostat and removable 8-inch diameter cryogenic deposition plate, (3) quartz crystal microbalance sensor, (4) inlet tube for water vapor, (5) feedthrough connected to a liquid nitrogen reservoir, (6) feedthrough connected to a rotary-vane pump, (7) C_{60} evaporation source with pneumatic shutter and (8)*

5

metal mesh above the water inlet. (b) Powder X-ray diffraction patterns (Cu Kα) at 95 K of pure ASW and C_{60} / H_2O mixtures with the indicated C_{60}:H_2O molar ratios. Tickmarks indicate the expected positions of ice Ih and C_{60} Bragg peaks. Minor contaminations with ice Ih can arise during the sample transfer in a humid atmosphere. Bragg peaks in the gray-shaded areas are due to the brass sample holder. (c) Photographic images of the 8-inch deposition plate under liquid nitrogen containing the 1:132 (left) and 1:48 deposits (right).

The pressure of the chamber was monitored with a combination Pirani / cold cathode pressure gauge (PenningVac PTF 90, Oerlikon Leybold Vacuum). The water-inlet system contained a needle valve (EV 016 DOS AB, Oerlikon Leybold Vacuum) to adjust the amount of dosed water vapor and a Pirani pressure sensor (Thermovac TTR91, Oerlikon Leybold Vacuum) was used to measure the water inlet pressure. Before each deposition, the C_{60} powder was degassed by heating to 250°C and waiting until the chamber reached base pressure (~2×10^{-6} mbar). The liquid water in the water reservoir was carefully degassed using at least three freeze-pump-thaw cycles.

The cryogenic deposition plate, which can be cooled to ~85 K with liquid nitrogen, was positioned 15 cm above the water inlet tube and the C_{60} evaporation source. The temperatures of the cryostat and the deposition plate were measured with K-type thermocouples using a home-made instrument built with an Adafruit Feather 32u4 Basic Proto microcontroller and two Adafruit MAX31856 Universal Thermocouple Amplifiers. The partial pressures of water were recorded using a mass spectrometer (Hiden HALO 100) containing a Faraday cup. For quartz-crystal microbalance (QCM) measurements, gold-plated AT-cut 6 MHz plano-convex quartz crystals (Sycon Instruments) were placed inside an Allectra 710-SH sensor firmly attached to the

center of the deposition plate. The QCM sensor was connected to a reflection bridge and a 0.5 –
60 MHz N2PK vector network analyzer through coaxial cables. The deposition rates were
monitored by recording the changes in the fundamental resonance frequency in the electrical
conductance data over time using the myVNA and QTZ softwares.[42]

Different compositions of the C_{60} / H_2O deposits were realized by either adjusting the
temperature of the C_{60} deposition source or the flow of water vapor into the chamber. Full details
on the calibration of the deposition rates based on QCM measurements are given in the
Supporting Information. The deposited C_{60} / H_2O mixtures had molar C_{60}:H_2O ratios of 1:1254,
1:452, 1:132, 1:48, 1:17 and 1:5.

To prepare samples for characterization outside the vacuum chamber, three-hour
deposition times were used. Following the deposition, the deposition plate was heated to ~125 K
under vacuum to reduce the surface area of the sample and thus avoid the formation of nitrogen
clathrate hydrates upon exposure to liquid nitrogen.[43] After cooling back to ~ 90 K, the sample
was extracted from the chamber under liquid nitrogen for further analysis as described in ref. 26.

Powder X-ray diffraction

After extraction from the vacuum chamber, the samples were transferred into custom-made
sample holders with Kapton windows under liquid nitrogen and mounted on a Stoe Stadi-P X-ray
transmission diffractometer (Cu Kα1, 40 kV, 30 mA, Ge(111)-monochromator) with a Mythen
1K linear detector. The data was collected from 2° – 60° in 5° steps (100 s per step). The
temperature of the samples was maintained initially at 95 K and then increased from 100 to 270
K in 10 K steps with a CryojetHT from Oxford Instruments.

Differential scanning calorimetry

The recovered samples were transferred into stainless-steel DSC pans. These were quickly transferred into a pre-cooled Perkin Elmer DSC 8000 Advanced Double-Furnace Differential Scanning Calorimeter and heated from 93 to 263 K at 10 K min^{-1} thus forming bulk ice Ih and C$_{60}$. A second heating scan was then recorded which was used for background subtraction. Finally, the ice was melted at 0°C. From the enthalpy of melting, the number of moles of H$_2$O were determined using a molar enthalpy of melting of 6012 J mol^{-1}.[44] The background-corrected DSC signal was then divided by the moles of H$_2$O and the heating rate, which yields a quantity in J mol^{-1} K^{-1}.

Temperature-programmed desorption (TPD) experiments

A deposition time of 2 hours was generally used for TPD experiments. After the deposition, the samples were maintained at ~90 K until the chamber base pressure was reached. The samples were then heated up to ~180 K while recording the partial pressure of H$_2$O (m/z = 18) with the mass spectrometer. The heating rates changed from ~2.5 K min^{-1} at 90 K to 1.0 K min^{-1} at 180 K. Upon reaching ~180 K, the upper pressure limit of the mass spectrometer was typically reached (1×10^{-4} mbar). In addition to the co-deposition experiments, a 'blanket' experiment was conducted for TPD analysis where a pure ASW film was deposited first for two hours (0.100 mbar inlet pressure) followed by two hours of C$_{60}$ deposition on top of the ice (evaporation source at 525°C). This corresponds to a bulk composition of 1 C$_{60}$:132 H$_2$O.

Scanning electron microscopy (SEM)

The C_{60} film from the blanket experiment was recovered after melting the sample and the ice-facing side of the film was imaged using a Jeol JSM-6700F scanning electron microscope. Additionally, the same amount of C_{60} was deposited directly onto an aluminum SEM stub firmly attached to the deposition plate.

Results and Discussion

The low-temperature X-ray diffraction (XRD) patterns shown in Fig. 1(b) demonstrate the amorphous nature of the pure ASW and the C_{60} / H_2O mixtures. Due to a very finely powdered nature and the associated difficulties transferring the sample into the sample holder, it was unfortunately not possible to record an XRD pattern of the 1:5 sample. Pure ASW displays a characteristic first strong diffraction peak at ~24° and a weaker feature around 43°.[2, 45-46] Upon increasing the C_{60} content, the diffraction patterns of the C_{60} / H_2O mixtures remain similar to pure ASW up to the 1:132 sample. An additional broad diffraction feature at ~29° emerges for the 1:48 sample. The diffraction pattern of the 1:17 sample is quite different to that of pure ASW, with a very broad feature around 21° and the ~29° feature, previously observed for the 1:48 sample, has grown more intense. It is important to note that none of these samples display Bragg peaks characteristic of bulk C_{60} (see Fig. S6).[47] Upon increasing the C_{60} content, the color of the samples changed from light pink for the sample with a molar C_{60}:H_2O ratio of 1:1254 to pink (1:452), red (1:132), dark red (1:48) and finally black for the two most C_{60}-rich samples (1:17 and 1:5). Photographic images of the 1:132 and 1:48 samples are shown in Fig. 1(c). Based on the diffraction data and the color changes, it can be concluded that C_{60} fullerene and H_2O have been successfully mixed over a large composition range using our cryogenic vapor co-deposition technique. This would be very difficult to achieve by any other method since the

solubility of C_{60} in liquid water is ~1×10^{-9} mol L^{-1} corresponding to a $1:6\times10^{10}$ molar $C_{60}:H_2O$ ratio.[48-49]

To investigate the effect of C_{60} on the crystallization properties of ASW, the various C_{60} / H_2O mixtures were heated in a differential scanning calorimeter (DSC) at 10 K min^{-1}. The resulting DSC scans, which were normalized with respect to the moles of H_2O present in each of the samples, are shown in Fig. 2(a). Consistent with the similarities in the XRD patterns, the DSC scans of the 1:1254, 1:452 and 1:132 samples resemble those of pure ASW with exotherms starting just above 150 K. The exotherm of pure ASW was found to be 1285 ± 93 J mol^{-1}, in good agreement with literature values.[46, 50-54] The onset temperatures and area of the exotherms were not found to change significantly upon increasing the C_{60} content from pure ASW to the 1:132 sample. This means that the presence of C_{60} does not have a significant effect on the crystallization of ASW in this composition range.
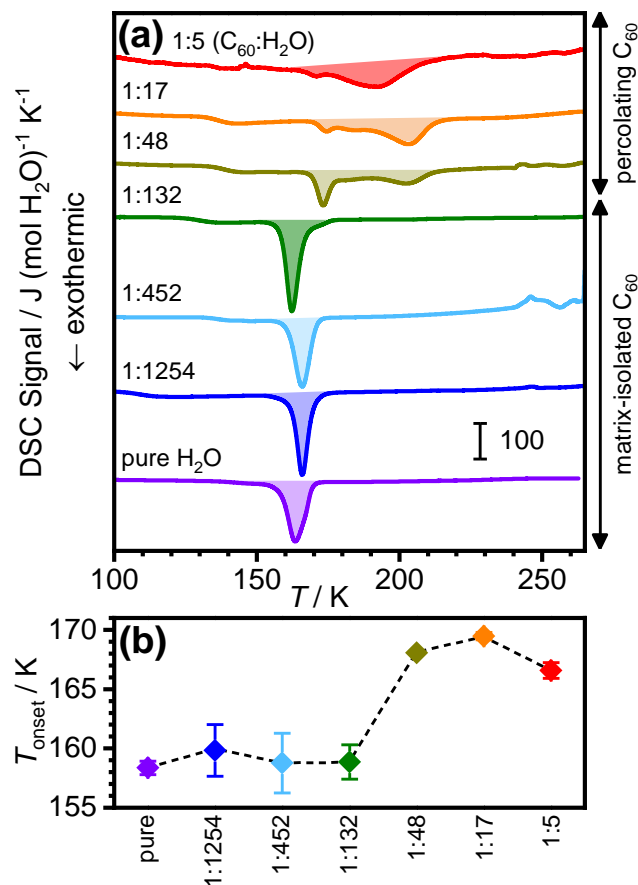
Figure 2. *(a) DSC scans of pure ASW and C_{60} / H_2O mixtures with the indicated C_{60}:H_2O molar ratios heated at 10 K min^{-1}. The DSC signals are normalized per mole H_2O. (b) Onset-temperatures of crystallization of the various samples.*

In the case of the more C_{60}-rich samples, an impact on the crystallization properties of H_2O can be seen. Firstly, the initial exotherm shifts by more than 10 K towards higher temperatures, as shown in Fig. 2(b), and decreases in area as the C_{60}:H_2O ratio changes from 1:48 and 1:17 to 1:5. Secondly, a second exothermic peak emerges at ~200 K for the 1:48 sample which increases in area and shifts towards lower temperatures for the 1:17 and 1:5 samples.

In addition to the crystallization of the H_2O, C_{60} can also be expected to crystallize upon heating either as it is expelled as the ASW matrix crystallizes or as amorphous C_{60} clusters

crystallize. Judging from the DSC data alone, it is not possible to tell at which temperatures the various processes take place. However, it is tempting to assign the low- and high-temperature exotherms to the crystallization of H_2O and C_{60}, respectively. The 1:48 sample was the first significantly darker sample, as shown in Fig. 1(c), and, based on computational studies, the first hydration shell of C_{60} is expected to contain 60 water molecules.[55-57] This means that the percolation threshold of C_{60}, corresponding to the transition from fully matrix-isolated C_{60} molecules to the formation of C_{60} aggregates with long-range connectivity, is reached between the 1:132 and 1:48 samples. Reassuringly, this agrees with theoretical estimates of contact networks of hard spheres, where the critical-volume fraction for percolation was determined to be 18.3%.[58] The volume percentages of C_{60} for the 1:132 and 1:48 mixtures are 14 and 31%, respectively, using molecular volumes of H_2O and C_{60} of 32.34 and 687.35 Å^{-3} calculated from the bulk densities.

It is important to emphasize that both exotherms were irreversible and therefore not observed upon second heating. Bulk C_{60} is known to display two reversible phase transitions: a glass transition-like transition around 90 K and a first-order transition at 260 K corresponding to the unfreezing of rotational motion.[59] The two phase transitions are endothermic[60-61] upon heating and not observed in our data which we attribute to the C_{60} being poorly crystalline with small domain sizes.

To investigate the crystallization processes upon heating in more detail, XRD patterns of the various samples were recorded as a function of temperature. The corresponding contour plots are shown in Fig. 3 for selected samples. The complete set of data are shown in Fig. S7 in the Supporting Information. The XRD data of pure ASW shown in Fig. 3(a) display the well-known sequence of irreversible phase transitions upon heating starting with the crystallization of ASW

to give stacking disordered ice (ice Isd) at ~140 K which is followed by its gradual conversion to the stable ice Ih above 180 K.[62] Consistent with the DSC data, increasing the C_{60} content from pure ASW to 1:132 does not lead to significant differences in the XRD data upon heating as shown in Fig. S7. This includes the cubicities (*i.e.* the percentage of cubic stacking)[63] of the ice Isd samples right after crystallization at 150 K as shown in Fig. S8. Specifically, the cubicities of the ice Isd obtained from pure ASW and the 1:1254, 1:452 and 1:132 samples at 150 K took values between 62.2 and 63.0% which is within the margins of error.[63]
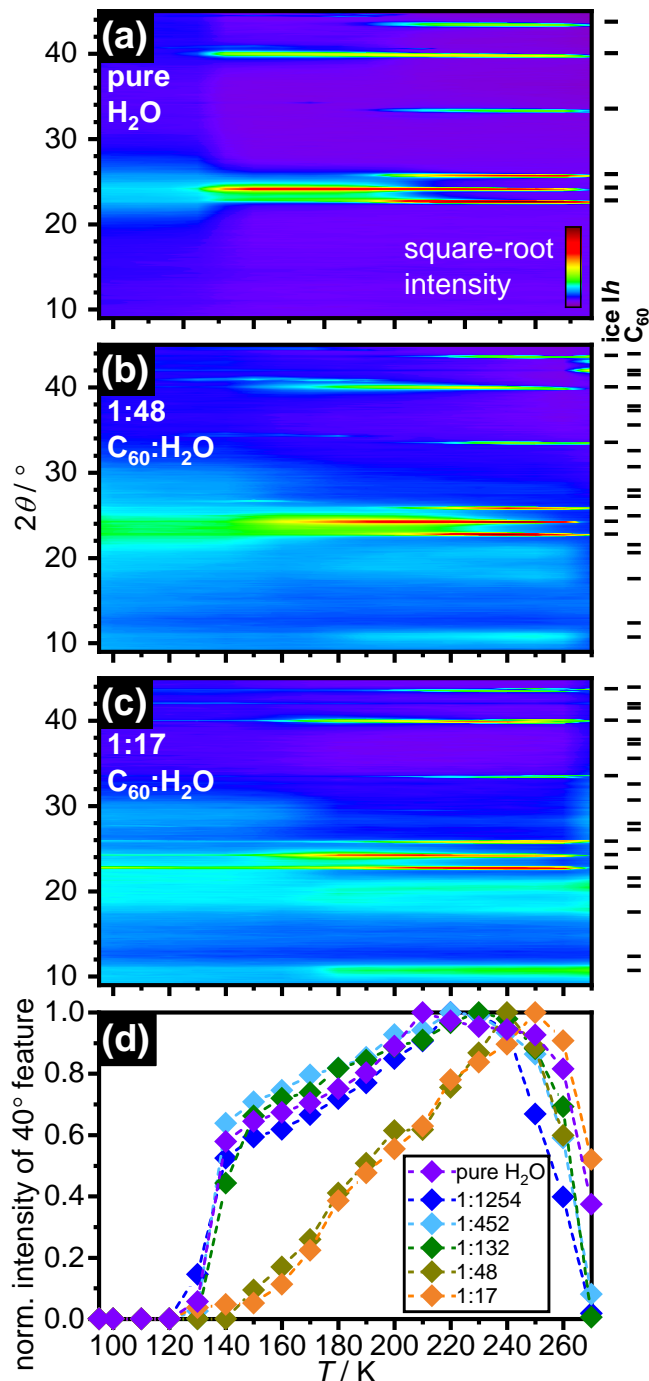
Figure 3. *X-ray diffraction data (Cu Kα) of pure ASW and C_{60} / H_2O mixtures upon heating. (a-c)*

Contour plots of X-ray diffraction patterns recorded upon heating from ~95 to 270 K in steps of 10 K. The

molar $C_{60}:H_2O$ ratios are indicated in (b,c). The diffraction intensities are shown on a square-root scale

to emphasize weaker features. Tick marks on the side of the panels indicate the expected positions for ice

Ih and C_{60} Bragg peaks. The complete set of diffraction data (including additional compositions) is shown

14

in Fig. S7 in the Supporting Information. (d) Intensities of the 40-degree ice I diffraction feature as function of temperature and normalized with respect to the most intense feature. This quantity was used to follow the crystallization of ASW.

Consistent with the previously-observed changes in the DSC data, the XRD data recorded upon heating started to change significantly with the 1:48 sample as shown in Fig. 3(b). The formation temperature of ice Isd shifts towards from ~130 K to ~160 K. Weak and broad Bragg peaks appear above ~185 K at 10.8, 17.9 and 20.6° which indicate the formation of small crystalline domains of C_{60} within the sample (see Fig. S6).[47] For the 1:17 sample, the C_{60} diffraction features are more intense and appear at slightly lower temperature compared to the 1:48 sample. In both cases, the appearance of C_{60} Bragg peaks is accompanied by the disappearance of diffraction intensity below 5° which is only observed for the two C_{60}-rich samples (see Fig. S7). This low-angle diffraction intensity is thought to arise from local density differences between H_2O and C_{60} regions on the length scale of nanometers. Its presence therefore provides evidence for the existence of percolating nanodomains of H_2O and C_{60}. Upon crystallization, the domain sizes increase significantly as the two components undergo phase separation which leads to the disappearance of the low-angle diffraction intensity and the appearance of C_{60} Bragg peaks.

Based on these findings, it is possible to firmly assign the low- and high-temperature exotherms in the DSC data to the crystallization of H_2O and C_{60}, respectively (see Fig 2). The decrease in temperature of the high-temperature exotherm is consistent with the appearance of C_{60} Bragg peaks at lower temperatures in the more C_{60}-rich samples. Obviously, if a sample contains more C_{60}, it is easier from a kinetic point of view to form more extended regions of crystalline C_{60}. Equally, in highly diluted samples, the concentration of C_{60} is simply too small to form large enough aggregates that can be detected with diffraction. As a side aspect of our study,

it should be possible to make C_{60} with very high surface areas upon freeze drying the samples with matrix-isolated C_{60}. The very small domain sizes of C_{60} obtained from the 1:18 sample at 270 K can be seen by comparing the half-widths of the Bragg peaks with those of bulk C_{60} (see Fig. S6).

Recently, pyrene was matrix-isolated in ASW at a 1:500 ratio.[37] In this study, the aggregation of pyrene was followed by detecting the excimer formation in fluorescence spectroscopy. It was found that the aggregation of pyrene coincides with the crystallization of ASW. The temperature difference between the H_2O and C_{60} crystallization observed here can be explained by the sensitivity of X-ray diffraction *vs.* fluorescence spectroscopy for detecting aggregation. While fluorescence spectroscopy can already detect the formation of dimeric aggregates, much more extended and crystalline regions are needed to give rise to Bragg peaks in diffraction experiments.

To follow the crystallization of H_2O in the various samples more quantitatively, the intensities of the (110) Bragg peaks at ~40° were analyzed as a function of temperature. Fig. 3(d) shows the obtained intensities normalized with respect to the highest intensity for each given sample which was typically observed at 220 K. Conveniently, the shape of this Bragg peak is not affected by the presence of stacking disorder and its intensity does not depend significantly on changes in the cubicity, at least within the 0 to 70% range as shown in Fig. S9. For pure ASW and the 1:1254, 1:452 and 1:132 samples, very similar trends were observed. The normalized peak intensities gain significant intensity between 130 and 140 K, which corresponds to the formation of ice I*sd* from ASW. After this, the peak intensities rise continuously up to ~210 K. Upon heating from 150 to 220 K, the half-width decreases from 0.470 to 0.319°. This suggests that the ice I*sd* domains increase continuously in size in this temperature range while also

16

transforming to ice Ih. It is noted that such changes in domain sizes have recently been predicted on the basis of vapor pressure measurements of ASW.[64] The much delayed intensity increases of the two C_{60}-rich samples can be explained by the presence of the percolating C_{60} domains that hinder the coalescence of ice I (ice Isd or ice Ih) domains. Essentially, the ice I is confined by the C_{60} domains. Owing to the presence of large amounts of C_{60} in those samples, it was not possible to accurately determine the cubicities of the ice Isd. The final drops in peak intensity above ~250 K observed for all samples may be due to the increases in the atomic thermal displacement parameters as the melting point is approached or simply to the fact that the samples drop in the sample holder as the ice grains soften.

As a next step, the effect of C_{60} on the desorption properties of H_2O vapor were investigated. For this, temperature-programmed desorption (TPD) experiments were carried out where the samples were heated in the vacuum chamber from ~85 to ~180 K. The partial pressure of water of pure ASW and the C_{60} / H_2O mixtures were recorded with a mass spectrometer (m/z = 18) as shown in Fig. 4(a). In the case of pure ASW, the partial pressure increases rapidly above ~130 K.[24, 26] As ASW crystallizes to ice Isd, the partial pressure decreases around ~150 K and then rises again above ~165 K as the vapor pressure of ice Isd increases with temperature.[24, 26] The TPD data of the 1:1254, 1:132 and 1:48 samples follow pure ASW closely, which means that the presence of C_{60} has no significant effect on the desorption of water in this composition range.

As mentioned in the Experimental section, the more C_{60}-rich samples were prepared by keeping the C_{60} deposition rate constant while reducing the amount of water vapor dosed into the chamber. Therefore, the partial pressures upon heating increase less compared to the previous experiments because there is less H_2O present in the depositions. In order to make the various

17

experiments comparable, the desorption peaks around 150 K were integrated against time in order to take variations in the heating rates into account and divided by the total mass of water dosed into the chamber. The resulting quantity reflects the amount of water desorption in the temperature range of ASW crystallization normalized with respect to the amount of deposited H_2O. Fig. 4(b) shows these quantities from all TPD experiments plotted against the volume percentage of C_{60} which is a convenient quantity for this comparison. The amounts of water desorption only begin to drop above 60 volume percent C_{60} (1:17 ratio), which implies that amounts of C_{60} significantly above the percolation threshold that are needed to suppress the water desorption.
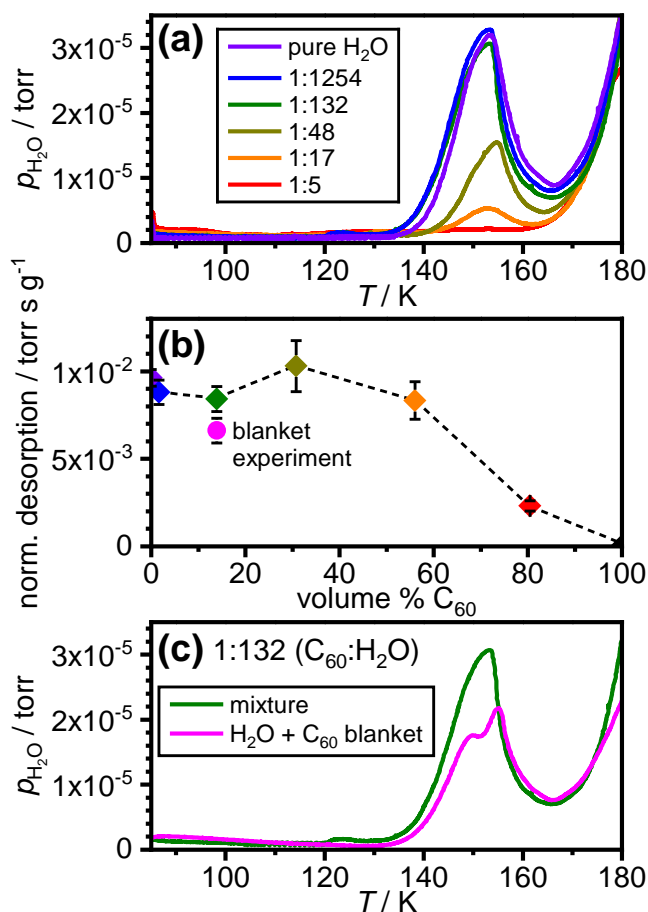
Figure 4. *Thermal desorption of H_2O vapor from C_{60} / H_2O mixtures upon heating. (a) Partial pressures of H_2O (m/z = 18) of pure ASW and various C_{60} / H_2O mixtures with the indicated C_{60}:H_2O*

molar ratios recorded upon heating. (b) Water desorption features integrated against time and normalized with respect to the mass of H_2O administered into the chamber during the vapor deposition experiment. (c) Comparison of desorption features of C_{60} / ASW mixtures and ASW covered with a blanket of C_{60}. The nominal bulk compositions of the two samples are 1:132 $C_{60}:H_2O$.

In an attempt to block the water vapor desorption more effectively, a 'blanket' of pure C_{60} was deposited on top of a pure ASW film so that the bulk composition of the entire sample was 1:132 $C_{60}:H_2O$. Based on the molecular volumes used earlier, this means that the thickness of the C_{60} layer was about 14% of the entire film. A comparison of the TPD data of the 'blanket' experiment with the corresponding 1:132 mixture is shown in Fig. 4(c). As can be seen from the data point in Fig. 4(b), the presence of the film leads to a ~21% reduction of the water desorption. The slight 'wiggle' in the TPD data of the blanket experiment at ~150 K could indicate some sudden rupturing of the C_{60} blanket as increasing amounts of desorbing H_2O vapor force their way through the C_{60} film. In any case, even if a C_{60} blanket is used, significant amounts of C_{60} are needed in order to suppress the water desorption. After the TPD experiment, the C_{60} film was recovered. A low-magnification scanning electron microscopy image of the ice-facing side is shown in Fig. 5. The film is significantly cracked most likely as a result of water-vapor permeation. To test if the cracks are due to the thermal treatment, a C_{60} film of the same thickness was deposited at 90 K directly onto a metal substrate and heated to room temperature. The SEM image of this sample shows a smooth surface (see Fig. S10).
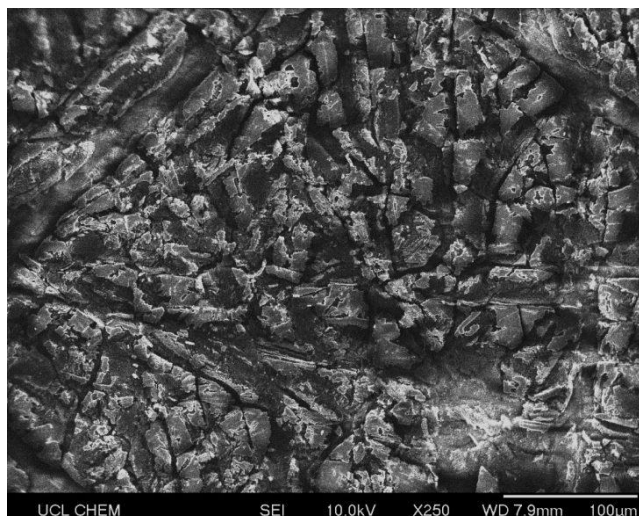
Figure 5. Low-magnification scanning electron microscopy image of the ASW-facing side of the C_{60} blanket after heating to ~180 K in vacuum.

Conclusions

The presence of matrix-isolated C_{60} appears to have no significant impact on the crystallization properties of ASW, including the cubicities of the ice I*sd* crystallization products. Upon reaching the percolation threshold of C_{60}, the onset temperature of crystallization of H_2O shifts towards higher temperatures by about 10 K. These findings illustrate the weak interaction between H_2O and C_{60}. The shift of the crystallization temperature above the percolation threshold is probably due to a physical confinement effect from the C_{60} which reduces the size of the H_2O domains. Small H_2O regions are physically separated, and they therefore crystallize independently.

The aggregation of C_{60} is seen as a separate process at higher temperature that shifts towards lower temperatures as the C_{60} content of the samples increases. In general, all crystallization processes of C_{60} / H_2O mixtures were found to be exothermic which is in stark contrast to the endothermic crystallization of ASW containing volatile guest species.[65]

The desorption of H_2O vapor in the temperature range of the crystallization of amorphous H_2O is not significantly affected by the presence of C_{60}, even for C_{60}-rich samples containing up to 60 volume percent C_{60}. This illustrates the force of water-vapor desorption that also seems to produce large cracks into a blanket of C_{60} covering a film of ASW. The presence of carbon species in ASW is thought to significantly increase its thermal-conductivity properties. On carbon-rich comets, the heat generated from local crystallization processes may therefore dissipate quickly to surrounding areas which combined with the strong evaporation power of H_2O may lead to the complex surface features observed during recent space missions.[19-20]

References

1. Burton, E. F.; Oliver, W. F., The Crystal Structure of Ice at Low Temperatures. *Proc. R. Soc. London, Ser. A* **1935**, *153*, 166-172.

2. Burton, E. F.; Oliver, W. F., X-Ray Diffraction Patterns of Ice. *Nature* **1935**, *135*, 505-506.

3. Tielens, A. G. G. M., The Molecular Universe. *Rev. Mod. Phys.* **2013**, *85*, 1021-1081.

4. Williams, D. A.; Fraser, H. J.; McCoustra, M. R. S., The Molecular Universe. *Astron. Geophys.* **2002**, *43*, 2.10-2.18.

5. De Sanctis, M. C., et al., The Diurnal Cycle of Water Ice on Comet 67p/Churyumov-Gerasimenko. *Nature* **2015**, *525*, 500-503.

6. Filacchione, G., et al., Exposed Water Ice on the Nucleus of Comet 67p/Churyumov–Gerasimenko. *Nature* **2016**, *529*, 368.

7. Gudipati, M. S., et al., Laboratory Studies Towards Understanding Comets. *Space Sci. Rev.* **2015**, *197*, 101-150.

8. Tielens, A. G. G. M.; Hagen, W., Model Calculations of the Molecular Composition of Interstellar Grain Mantles. *Astron. Astrophys.* **1982**, *114*, 245-260.

9. Ehrenfreund, P.; Foing, B. H., Fullerenes in Space. *Adv. Space Res.* **1997**, *19*, 1033-1042.

10. Foing, B. H.; Ehrenfreund, P., Detection of Two Interstellar Absorption Bands Coincident with Spectral Features of C60+. *Nature* **1994**, *369*, 296-298.

11. Cami, J.; Bernard-Salas, J.; Peeters, E.; Malek, S. E., Detection of C_{60} and C_{70} in a Young Planetary Nebula. *Science* **2010**, *329*, 1180.

12. Radicati di Brozolo, F.; Bunch, T. E.; Fleming, R. H.; Macklin, J., Fullerenes in an Impact Crater on the Ldef Spacecraft. *Nature* **1994**, *369*, 37-40.

13. Becker, L.; Bunch, T. E., Fullerenes, Fulleranes and Polycyclic Aromatic Hydrocarbons in the Allende Meteorite. *Meteorit. Planet. Sci.* **1997**, *32*, 479-487.

14. Tielens, A. G. G. M., The Molecular Universe. *Reviews of Modern Physics* **2013**, *85*, 1021-1081.

15. Sunshine, J. M.; Groussin, O.; Schultz, P. H.; A'Hearn, M. F.; Feaga, L. M.; Farnham, T. L.; Klaasen, K. P., The Distribution of Water Ice in the Interior of Comet Tempel 1. *Icarus* **2007**, *190*, 284-294.

16. Capaccioni, F., et al., The Organic-Rich Surface of Comet 67p/Churyumov-Gerasimenko as Seen by Virtis/Rosetta. *Science* **2015**, *347*.

17. Jorda, L., et al., The Global Shape, Density and Rotation of Comet 67p/Churyumov-Gerasimenko from Preperihelion Rosetta/Osiris Observations. *Icarus* **2016**, *277*, 257-278.

18. Weissman, P., Sink Holes and Dust Jets on Comet 67p. *Nature* **2015**, *523*, 42-43.

19. Sierks, H., et al., On the Nucleus Structure and Activity of Comet 67p/Churyumov-Gerasimenko. *Science* **2015**, *347*, aaa1044.

20. Herique, A.; Kofman, W.; Zine, S.; Blum, J.; Vincent, J.-B.; Ciarletti, V., Homogeneity of 67p/Churyumov-Gerasimenko as Seen by Consert: Implication on Composition and Formation. *Astron. Geophys.* **2019**, *630*, A6.

21. Lauretta, D. S., et al., The Osiris-Rex Target Asteroid (101955) Bennu: Constraints on Its Physical, Geological, and Dynamical Nature from Astronomical Observations. *Meteorit. Planet. Sci.* **2015**, *50*, 834-849.

22. Tachibana, S., et al., Hayabusa2: Scientific Importance of Samples Returned from C-Type near-Earth Asteroid (162173) 1999 Ju$_3$. *Geochem. J.* **2014**, *48*, 571-587.

23. Notesco, G.; Bar-Nun, A.; Owen, T., Gas Trapping in Water Ice at Very Low Deposition Rates and Implications for Comets. *Icarus* **2003**, *162*, 183-189.

24. Smith, R. S.; Petrik, N. G.; Kimmel, G. A.; Kay, B. D., Thermal and Nonthermal Physiochemical Processes in Nanoscale Films of Amorphous Solid Water. *Acc. Chem. Res.* **2012**, *45*, 33-42.

25. Smith, R. S.; May, R. A.; Kay, B. D., Desorption Kinetics of Ar, Kr, Xe, N2, O2, Co, Methane, Ethane, and Propane from Graphene and Amorphous Solid Water Surfaces. *J. Phys. Chem. B* **2016**, *120*, 1979-1987.

26. Talewar, S. K.; Halukeerthi, S. O.; Riedlaicher, R.; Shephard, J. J.; Clout, A. E.; Rosu-Finsen, A.; Williams, G. R.; Langhoff, A.; Johannsmann, D.; Salzmann, C. G., Gaseous "Nanoprobes" for Detecting Gas-Trapping Environments in Macroscopic Films of Vapor-Deposited Amorphous Ice. *J. Chem. Phys.* **2019**, *151*, 134505.

27. Guennoun, Z.; Aupetit, C.; Mascetti, J., Photochemistry of Coronene with Water at 10 K: First Tentative Identification by Infrared Spectroscopy of Oxygen Containing Coronene Products. *Phys. Chem. Chem. Phys.* **2011**, *13*, 7340-7347.

28. Guennoun, Z.; Aupetit, C.; Mascetti, J., Photochemistry of Pyrene with Water at Low Temperature: Study of Atmospherical and Astrochemical Interest. *J. Phys. Chem. A* **2011**, *115*, 1844-1852.

29. Bouwman, J.; Mattioda, A. L.; Linnartz, H.; Allamandola, L. J., Photochemistry of Polycyclic Aromatic Hydrocarbons in Cosmic Water Ice. *Astron. Astrophys.* **2011**, *525*.

30. Cook, A. M.; Ricca, A.; Mattioda, A. L.; Bouwman, J.; Roser, J.; Linnartz, H.; Bregman, J.; Allamandola, L. J., Photochemistry of Polycyclic Aromatic Hydrocarbons in Cosmic Water Ice: The Role of Pah Ionization and Concentration. *Astrophys. J.* **2015**, *799*, 14.

31. de Barros, A. L. F.; Mattioda, A. L.; Ricca, A.; Cruz-Diaz, G. A.; Allamandola, L. J., Photochemistry of Coronene in Cosmic Water Ice Analogs at Different Concentrations. *Astrophys. J.* **2017**, *848*, 112.

32. Michoulier, E.; Toubin, C.; Simon, A.; Mascetti, J.; Aupetit, C.; Noble, J. A., Perturbation of the Surface of Amorphous Solid Water by the Adsorption of Polycyclic Aromatic Hydrocarbons. *J. Phys. Chem. C* **2020**, *124*, 2994-3001.

33. Courty, A.; Mons, M.; Dimicoli, I.; Piuzzi, F.; Gaigeot, M.-P.; Brenner, V.; de Pujo, P.; Millié, P., Quantum Effects in the Threshold Photoionization and Energetics of the Benzene−H2o and Benzene−D2o Complexes: Experiment and Simulation. *J. Phys. Chem. A* **1998**, *102*, 6590-6600.

34. Ruiterkamp, R.; Peeters, Z.; Moore, M. H.; Hudson, R. L.; Ehrenfreund, P., A Quantitative Study of Proton Irradiation and Uv Photolysis of Benzene in Interstellar Environments. *Astron. Astrophys.* **2005**, *440*, 391-402.

35. Marchione, D.; Thrower, J. D.; McCoustra, M. R. S., Efficient Electron-Promoted Desorption of Benzene from Water Ice Surfaces. *Phys. Chem. Chem. Phys.* **2016**, *18*, 4026-4034.

36. Dawes, A.; Pascual, N.; Mason, N. J.; Gärtner, S.; Hoffmann, S. V.; Jones, N. C., Probing the Interaction between Solid Benzene and Water Using Vacuum Ultraviolet and Infrared Spectroscopy. *Phys. Chem. Chem. Phys.* **2018**, *20*, 15273-15287.

37. Lignell, A.; Gudipati, M. S., Mixing of the Immiscible: Hydrocarbons in Water-Ice near the Ice Crystallization Temperature. *J. Phys. Chem. A* **2015**, *119*, 2607-2613.

38. Fisher, M.; Devlin, J. P., Defect Activity in Amorphous Ice from Isotopic Exchange Data: Insight into the Glass Transition. *J. Phys. Chem.* **1995**, *99*, 11584-11590.

39. Shephard, J. J.; Evans, J. S. O.; Salzmann, C. G., Structural Relaxation of Low-Density Amorphous Ice Upon Thermal Annealing. *J. Phys. Chem. Lett.* **2013**, *4*, 3672-3676.

40. Shephard, J. J.; Salzmann, C. G., Molecular Reorientation Dynamics Govern the Glass Transitions of the Amorphous Ices. *J. Phys. Chem. Lett.* **2016**, *7*, 2281-2285.

41. Shephard, J. J. Structure-Property Relationships in Two-Component Liquids. PhD thesis, Durham University, 2014.

42. Johannsmann, D., Viscoelastic, Mechanical, and Dielectric Measurements on Complex Samples with the Quartz Crystal Microbalance. *Phys. Chem. Chem. Phys.* **2008**, *10*, 4516-4534.

43. Mayer, E.; Hallbrucker, A., Unexpectedly Stable Nitrogen and Oxygen Clathrate Hydrates from Vapour Deposited Amorphous Solid Water. *J. Am. Chem. Soc.* **1989**, *12*, 749-751.

44. Feistel, R.; Wagner, W., A New Equation of State for H2o Ice Ih. *J. Phys. Chem. Ref. Data* **2006**, *35*, 1021-1047.

45. Dowell, L. G.; Rinfret, A. P., Low-Temperature Forms of Ice as Studied by X-Ray Diffraction. *Nature* **1960**, *188*, 1144-1148.

46. Hallbrucker, A.; Mayer, E.; Johari, G. P., Glass-Liquid Transition and the Enthalpy of Devitrification of Annealed Vapor-Deposited Amorphous Solid Water: A Comparison with Hyperquenched Glassy Water. *J. Phys. Chem.* **1989**, *93*, 4986-4990.

47. Heiney, P. A.; Fischer, J. E.; McGhie, A. R.; Romanow, W. J.; Denenstein, A. M.; McCauley Jr, J. P.; Smith, A. B.; Cox, D. E., Orientational Ordering Transition in Solid C_{60}. *Phys. Rev. Lett.* **1991**, *66*, 2911-2914.

48. Ma, X.; Wigington, B.; Bouchard, D., Fullerene C60: Surface Energy and Interfacial Interactions in Aqueous Systems. *Langmuir* **2010**, *26*, 11886-11893.

49. Fortner, J. D., et al., C60 in Water: Nanocrystal Formation and Microbial Response. *Environ. Sci. Technol.* **2005**, *39*, 4307-4316.

50. Ghormley, J. A., Enthalpy Changes and Heat-Capacity Changes in the Transformations from High-Surface-Area Amorphous Ice to Stable Hexagonal Ice. *J. Chem. Phys.* **1968**, *48*, 503-508.

51. MacFarlane, D. R.; Angell, C. A., Nonexistent Glass Transition for Amorphous Solid Water. *J. Phys. Chem.* **1984**, *88*, 759-762.

52. Floriano, M. A.; Handa, Y. P.; Klug, D. D.; Whalley, E., Nature of the Transformations of Ice I and Low-Density Amorphous Ice to High-Density Amorphous Ice. *J. Chem. Phys.* **1989**, *91*, 7187-7192.

53. Hallbrucker, A.; Mayer, E., Calorimetric Study of the Vitrified Liquid Water to Cubic Ice Phase Transition. *J. Phys. Chem.* **1987**, *91*, 503-505.

54. Johari, G. P.; Fleissner, G.; Hallbrucker, A.; Mayer, E., Thermodynamic Continuity between Glassy and Normal Water. *J. Phys. Chem.* **1994**, *98*, 4719-4725.

55. Scharff, P., et al., Structure of C60 Fullerene in Water: Spectroscopic Data. *Carbon* **2004**, *42*, 1203-1206.

56. Ludwig, R.; Appelhagen, A., Calculation of Clathrate-Like Water Clusters Including H2o-Buckminsterfullerene. *Angew. Chem. Int. Ed.* **2005**, *44*, 811-815.

57. Hernández-Rojas, J.; Bretón, J.; Gomez Llorente, J. M.; Wales, D. J., Global Potential Energy Minima of C60(H2o)N Clusters. *J. Phys. Chem. B* **2006**, *110*, 13357-13362.

58. Powell, M. J., Site Percolation in Randomly Packed Spheres. *Phys. Rev. B* **1979**, *20*, 4194-4198.

59. David, W. I. F.; Ibberson, R. M.; Dennis, T. J. S.; Hare, J. P.; Prassides, K., Structural Phase Transitions in the Fullerene C 60. *EPL* **1992**, *18*, 219-225.

60. Tse, J. S.; Klug, D. D.; Wilkinson, D. A.; Handa, Y. P., Phase Transitions in Solid C60. *Chem. Phys. Lett.* **1991**, *183*, 387-390.

61. Matsuo, T.; Suga, H.; David, W. I. F.; Ibberson, R. M.; Bernier, P.; Zahab, A.; Fabre, C.; Rassat, A.; Dworkin, A., The Heat Capacity of Solid C60. *Solid State Comm.* **1992**, *83*, 711-715.

62. Kuhs, W. F.; Sippel, C.; Falentya, A.; Hansen, T. C., Extent and Relevance of Stacking Disorder in "Ice I*c*". *Proc. Natl. Acad. Sci. USA* **2012**, *109*, 21259-21264.

63. Malkin, T. L.; Murray, B. J.; Salzmann, C. G.; Molinero, V.; Pickering, S. J.; Whale, T. F., Stacking Disorder in Ice I. *Phys. Chem. Chem. Phys.* **2015**, *17*, 60-76.

64. Nachbar, M.; Duft, D.; Leisner, T., Volatility of Amorphous Solid Water. *J. Phys. Chem. B* **2018**, *122*, 10044-10050.

65. Kouchi, A.; Sirono, S.-i., Crystallization Heat of Impure Amorphous H_2o Ice. *Geophys. Res. Lett.* **2001**, *28*, 827-830.

TOC Graphic

matrix-isolated C$_{60}$ → percolating C$_{60}$
amorphous ice